Electromagnetic Modeling of PCB Based on Darwin's Model Combined With Degenerated Prism Whitney Elements

Houssein Taha, Thomas Henneron, Zuqi Tang, Yvonnick Le Menach, Loris Pace, and Jean-Pierre Ducreux, *Member, IEEE*

***Abstract*—Due to the advancement in the development of semiconductors used in the power converters, the printed circuit boards (PCBs) require an in-depth study of their electromagnetic behavior. To characterize the behavior of the PCBs, the Darwin model is employed, which can take into account all the coupled effects, namely resistive, inductive, and capacitive effects, at the intermediate frequencies. Nevertheless, the study of particular structures having a geometric dimension smaller than the others can create meshing difficulties. The modeling of thin structures by the finite element method requires the optimization of the mesh. To circumvent this issue, the shell elements for both node and edge elements are applied in this work. Finally, to validate the proposed approaches, two PCBs with different geometries are studied in both time and frequency domains, where the measurements for a single PCB are provided to compare with the numerical results.**

***Index Terms*—Electromagnetic fields, finite element (FE) method, resistive–inductive–capacitive effects, shell elements, thin structures.**

I. Introduction

THE requirements for power converters in embedded systems, such as automobiles and aerospace, have increased in importance recently. In addition, due to the development of wide bandgap semiconductors used in these converters, the frequency of voltage and current waveforms becomes increasingly significant. Then, the electromagnetic behavior of the printed circuit boards (PCBs) used to make up power electronic converters cannot be neglected in comparison with semiconductors and passive components. To design efficiently a PCB, numerical modeling can be used to characterize its electromagnetic behavior. Nevertheless, the modeling of PCB presents several numerical issues.

Manuscript received 5 April 2022; revised 24 June 2022; accepted 23 July 2022. Date of publication 5 August 2022; date of current version 10 October 2022. This work was supported by the European Regional Development Fund (ERDF) NP0017752 and LAMEL laboratory (joint laboratory between the L2EP laboratory and the EDF company). Recommended for publication by Associate Editor A. Lindemann. *(Corresponding author: Thomas Henneron.)*

Houssein Taha, Thomas Henneron, Zuqi Tang, Yvonnick Le Menach, and Loris Pace are with the Univ. Lille, Arts et Metiers Institute of Technology, Centrale Lille, Junia, ULR2697-L2EP, F-59000 Lille, France (e-mail: houssein.taha@univ-lille.fr; thomas.henneron@univ-lille.fr; zuqi.tang@univ-lille.fr; yvonnick.le-menach@univ-lille.fr; loris.pace@ec-lyon.fr).

Jean-Pierre Ducreux is with the EDF R&D, ERMES, 91120 Palaiseau, France (e-mail: jean-pierre.ducreux@edf.fr).

Color versions of one or more figures in this article are available at https://doi.org/10.1109/TPEL.2022.3196749.

Digital Object Identifier 10.1109/TPEL.2022.3196749

Based on a numerical approach, such as the finite element (FE) method, resistive, capacitive, and inductive effects associated with a PCB should be studied simultaneously when the frequency of excitations increases. Recently, the quasi-static Darwin model, which is a substitute for the full Maxwell system except it neglects wave propagation, has attracted more and more attention in the research area [1]–[5].

Nevertheless, due to the small size of the tracks, the modeling of a three-dimensional (3-D) PCB presents many difficulties in the electromagnetic domain. The significant contrast existing in the modeling of thin structures, such as the PCBs, causes difficulties in the generation of meshes. Moreover, this disproportion leads to undesirable elements, in particular, the flat elements. Consequently, the solving of the resulting FE matrix becomes more difficult since the conditioning number of the matrix becomes worse. Otherwise, an extremely fine mesh is required to avoid the flat elements; therefore, the FE computation becomes more expensive in both memory and computational time.

Besides, the meshing of the thin structures by modeling them in surfaces without thickness is a solution introduced in the literature. Generally, the electromagnetic modeling of structures including thin shell models and thin wires is a complex problem in the fields of electrical engineering [6]–[8]. The shell element method consists in representing the thin structures by 2-D surfaces. This can be done by developing suitable formulations according to the field continuity conditions through thin structures [6], [8], [9]. These formulations can be solved using either the boundary element method [7], [10], the FE method [11]–[14] or the integral method, such as the partial element equivalent circuit (PEEC) method [15], [16].

The PEEC method is well known as an effective modeling method in the power electronics and electrical engineering domains. It applies to a wide range of devices: PCBs, busbars, and solid conductors. The standard PEEC approach was only addressed to conductive or dielectric materials with structured meshes where the coupled resistive–inductive effects are taken into account by the magneto-quasi-static model and the capacitive effects by the electrostatic one. In [16], in order to reduce the number of unknowns, a surface-based PEEC formulation is developed taken into account the conductors and dielectrics materials. In [17] and [18], different approaches are applied to reduce the computational time based on the adaptive cross

approximation and singular value decomposition methods for frequency problem and on a multipoint model order reduction for full-wave problem, respectively. Recently, the PEEC method has been generalized to any type of FE mesh [19], and the full Maxwell system is solved without any assumption where the conductive, dielectric, and magnetic materials are considered. In addition, a formulation equivalent to the Darwin model has been developed in [20] to take into account the resistive, inductive, and capacitive effects simultaneously at intermediate frequencies but without the presence of magnetic materials.

Compared to the FE method, PEEC has several advantages. The air region does not meshed because it is treated by integral equations that reduce the mesh size. On the other hand, the PEEC method leads to full matrices that introduce solving difficulties in the case of fine meshes. Consequently, preconditioned iterative solvers have to be used, where the construction of effective preconditioners is not trivial, in particular, at high frequency.

The use of FE computation codes often leads to sparse linear systems that can reach sizes of tens of millions of unknowns [21]. The solving of these systems has the disadvantage of leading to prohibitive costs in CPU time and memory space, in particular, in the case of the Darwin model. Besides, two formulations derived from the Darwin model have been proposed in our previous work to address the instability and the asymmetric issues [3] and the computational limitations linked to the huge degrees of freedom (DoF) of industrial problems [21].

Concerning the numerical modeling of the thin regions with the FE method, a lot of research has been carried out. The applications have been seen for the computation of eddy currents in thin conductive shells [8], [11] for the computation of the magnetostatic field in thin magnetic sheets [11] and also for the modeling of thin cracks. Most approaches lead to use a kind of double-layer nodal-based shell elements [8], [9] but they are only suitable for interpolating scalar variables. On the other hand, a thin shell eddy current problem is solved using the nodal and the edge version for the discretization of scalar and vector variables, respectively [12], [22], [23]. In particular, the shell element method provides a more general description of the physical phenomena without any particular hypothesis about the fields inside the thin structure. In addition, it allows a 3-D distribution of the electromagnetic fields.

In this article, the Darwin model is solved by integrating the shell element method to further reduce the computational cost, applied to both node and edge elements. They are derived from the degeneration of Whitney prismatic elements [12], [22] and they can be applied to the different quasi-static formulations.

Following this introduction, the full-wave Maxwell system is briefly introduced in Section II. In Section III, the Darwin model is presented in fields and potentials formulation, where the discretized matrix system of the Darwin model in time and frequency domains is given in Section IV. In Section V, the shell element method is presented. Numerical examples, including measurement results, are used to study the electromagnetic behavior of PCBs in both frequency and time domains in Section VI. Finally, our conclusion is given in Section VII.

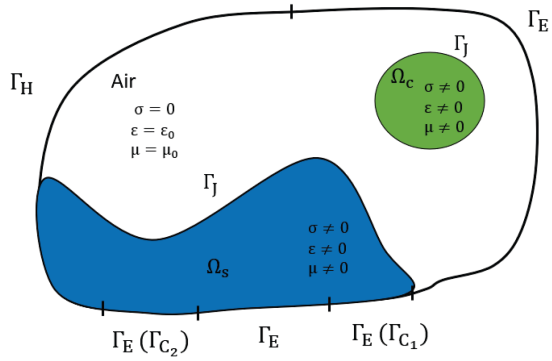

Fig. 1. Studied domain.

II. Maxwell's System

Let us consider $\Omega \subset \mathbb{R}^3$ an open connected domain. $\Omega_c \subset \Omega$ presents the 3-D conductive subdomain and $\Omega_s \subset \Omega$ presents the subdomain of the 2-D conductive thin structures, as shown in Fig. 1.

The full Maxwell system in the time domain, given as follows, describes the magnetic and electric behaviors of the electromagnetic device with no free electric charges.

$$\nabla \times \mathbf{E} = -\frac{\partial \mathbf{B}}{\partial t} \tag{1}$$

$$\nabla \times \mathbf{H} = \mathbf{J} + \frac{\partial \mathbf{D}}{\partial t} \tag{2}$$

$$\nabla \cdot \mathbf{B} = 0 \tag{3}$$

$$\nabla \cdot \mathbf{D} = 0. \tag{4}$$

The boundary Γ of domain Ω is decomposed into two complementary parts denoted Γ_H and Γ_E such that $\Gamma_H \cap \Gamma_E = \emptyset$ and $\Gamma = \Gamma_H \cup \Gamma_E = \partial\Omega$. Then, the boundary conditions on $\mathbf{E}$ and $\mathbf{H}$ are written as follows:

$$\Gamma_E : \mathbf{E} \times \mathbf{n} = \mathbf{0} \tag{5}$$

$$\Gamma_H : \mathbf{H} \times \mathbf{n} = \mathbf{0}. \tag{6}$$

The relations between (1) and (5) introduce a boundary condition on $\mathbf{B}$ such as

$$\Gamma_E : \mathbf{B} \cdot \mathbf{n} = 0 \tag{7}$$

and the relations between (2) and (6) introduce boundary conditions on $\mathbf{J}$ and $\mathbf{D}$ such as

$$\Gamma_H : \mathbf{J} \cdot \mathbf{n} = 0 \tag{8}$$

$$\Gamma_H : \mathbf{D} \cdot \mathbf{n} = 0. \tag{9}$$

In addition, on the internal boundary of the subdomains Ω_c and Ω_s, a supplementary condition is imposed such that

$$\Gamma_J : \mathbf{J} \cdot \mathbf{n} = 0. \tag{10}$$

The equations defined above are followed by the behavior laws of materials

$$\mathbf{B} = \mu \mathbf{H} \tag{11}$$

$$\mathbf{J} = \sigma \mathbf{E} \tag{12}$$

$$\mathbf{D} = \varepsilon \mathbf{E} \tag{13}$$

where $\mathbf{E}$ is the electric field (V/m), $\mathbf{H}$ is the magnetic field $(\mathrm{A/m})$, $\mathbf{B}$ is the magnetic flux density (T), $\mathbf{J}$ is the current density $(\mathrm{A/m^2})$, $\mathbf{D}$ is the electric flux density $(\mathrm{C/m^2})$, μ is the magnetic permeability, and σ and ε are the electric conductivity and permittivity, respectively.

III. Darwin Model

By the Helmholtz decomposition, the electric field $\mathbf{E}$ can be split into two parts, an irrotational part $\mathbf{E}_{\mathrm{irr}}$, which is curl-free, and a solenoidal part $\mathbf{E}_{\mathrm{sol}}$, which is divergence-free [24]

$$\mathbf{E} = \mathbf{E}_{\mathrm{irr}} + \mathbf{E}_{\mathrm{sol}},\ \nabla \times \mathbf{E}_{\mathrm{irr}} = \mathbf{0},\ \nabla \cdot \mathbf{E}_{\mathrm{sol}} = 0. \tag{14}$$

By neglecting the rotational part of the displacement current $\partial(\varepsilon \mathbf{E}_{\mathrm{sol}})/\partial t$, which is responsible for wave propagation, the Darwin model reads as follows:

$$\nabla \times \mathbf{E}_{\mathrm{sol}} = -\frac{\partial \mathbf{B}}{\partial t} \tag{15}$$

$$\nabla \times \mathbf{H} = \mathbf{J} + \frac{\partial(\varepsilon \mathbf{E}_{\mathrm{irr}})}{\partial t} \tag{16}$$

$$\nabla \cdot \mathbf{B} = 0 \tag{17}$$

$$\nabla \cdot \mathbf{J} = 0 \tag{18}$$

$$\nabla \cdot (\varepsilon \mathbf{E}_{\mathrm{irr}}) = 0. \tag{19}$$

From (17), the magnetic vector potential (MVP) $\mathbf{A}$ can be introduced such as

$$\mathbf{B} = \nabla \times \mathbf{A} \tag{20}$$

$$\mathbf{A} \times \mathbf{n} = \mathbf{0} \ \text{on}\, \Gamma_{\mathrm{E}}. \tag{21}$$

Combining (20) with (15), by introducing the electric scalar potential (ESP) φ, which is defined in the whole domain, the electric field $\mathbf{E}$ is given as follows:

$$\mathbf{E} = -\frac{\partial \mathbf{A}}{\partial t} - \nabla \varphi - \sum_{j=1}^{N_\alpha} V_{\mathrm{s_j}} \nabla \alpha_{\mathrm{j}} \tag{22}$$

$$\varphi = 0 \ \ \text{on}\, \Gamma_{\mathrm{E}} \tag{23}$$

where $V_{\mathrm{s_j}}$ is a fixed scalar potential on the boundary $\Gamma_{\mathrm{C_j}}$, N_α is the number of sources, and the ESP α_{j} is an arbitrary nonzero source satisfying

$$\alpha_{\mathrm{j}} = 1 \ \text{ on } \ \Gamma_{\mathrm{C_j}} \quad \text{and } \ 0 \ \text{ elsewhere.}$$

From (14), $\mathbf{E}_{\mathrm{irr}}$ can be represented as a function of the ESP φ and $V_{\mathrm{s_j}}$ while $\mathbf{E}_{\mathrm{sol}}$ can be expressed as a function of the MVP $\mathbf{A}$

$$\mathbf{E}_{\mathrm{irr}} = -\nabla \varphi - \sum_{j=1}^{N_\alpha} V_{\mathrm{s_j}} \nabla \alpha_{\mathrm{j}} \ \text{ and } \ \mathbf{E}_{\mathrm{sol}} = -\frac{\partial \mathbf{A}}{\partial t}. \tag{24}$$

We now replace the expressions (20) and (24) in (16). Then, by considering a single fixed potential V_{s}, Ampère's equation reduces to the Darwin–Ampère's equation

$$\begin{aligned} \nabla \times (\nu \nabla \times \mathbf{A}) + \sigma \left(\frac{\partial \mathbf{A}}{\partial t} + \nabla \varphi \right) + \frac{\partial}{\partial t}(\varepsilon \nabla \varphi) \\ = -\sigma V_{\mathrm{s}} \nabla \alpha - \frac{\partial V_{\mathrm{s}}}{\partial t}(\varepsilon \nabla \alpha). \end{aligned} \tag{25}$$

By applying of the divergence operator to the Darwin–Ampère equation (25), the charge conservation equation is written in Ω as follows:

$$\begin{aligned} \nabla \cdot \left(\sigma \left(\frac{\partial \mathbf{A}}{\partial t} + \nabla \varphi \right) + \frac{\partial}{\partial t}(\varepsilon \nabla \varphi) \right) \\ = -\nabla \cdot \left(\sigma V_{\mathrm{s}} \nabla \alpha + \frac{\partial V_{\mathrm{s}}}{\partial t}(\varepsilon \nabla \alpha) \right) \end{aligned} \tag{26}$$

where ν is the magnetic reluctivity (the inverse of the magnetic permeability μ). Equations (25) and (26) make up the classical $\mathbf{A}/\varphi$ potential formulation for the Darwin model [2] with a single fixed potential V_{s}.

IV. Discrete Darwin Model

A spatial discretization of (25) and (26) is given in the following. The edge element is adopted for the MVP $\mathbf{A}$, and the nodal element is adopted for the ESP φ.

The unknowns are carried by $\varphi_i,\ i = (1, \ldots, N_n)$, and $A_i,\ i = (1, \ldots, N_e)$, where N_n and N_e are the number of the nodes and edges, respectively. Let $\mathbf{X}_\varphi \in \mathbb{R}^{N_n}$ and $\mathbf{X}_{\mathbf{A}} \in \mathbb{R}^{N_e}$ be the component vectors of φ_i and A_i, respectively, we introduce the decomposition of φ and $\mathbf{A}$ in their canonical basis

$$\varphi = \sum_{i=1}^{N_n} \varphi_i w_i^0,\ \mathbf{A} = \sum_{i=1}^{N_e} A_i \mathbf{w}_i^1$$

with w_i^0 and $\mathbf{w}_i^1$ the nodal and edge interpolation functions.

In the time domain, by using the implicit Euler scheme for the first derivatives $\partial \mathbf{A}/\partial t$ and $\partial \varphi/\partial t$, the discrete Darwin equations can be rewritten as a first-order differential-algebraic system of equations with a time step $\Delta t := t^{n+1} - t^n$

$$\begin{aligned} &\begin{bmatrix} \mathbb{M}_1 & \mathbb{M}_2 \\ \dfrac{1}{\Delta t}\mathbb{L}_\sigma & \mathbb{M}_3 \end{bmatrix} \begin{bmatrix} \mathbf{X}_{\mathbf{A}} \\ \mathbf{X}_\varphi \end{bmatrix}^{n+1} \\ &= -\begin{bmatrix} \mathbf{F}_{\mathbf{A}}(\mathbf{t}) \\ \mathbf{F}_\varphi(t) \end{bmatrix}^n + \frac{1}{\Delta t} \begin{bmatrix} \mathbb{K}_\sigma & \mathbb{L}_\varepsilon \\ \mathbb{L}_\sigma & \mathbb{G}_\varepsilon \end{bmatrix} \begin{bmatrix} \mathbf{X}_{\mathbf{A}} \\ \mathbf{X}_\varphi \end{bmatrix}^n \end{aligned} \tag{27}$$

with

$$\mathbb{M}_1 = \mathbb{M}_\nu + \frac{1}{\Delta t}\mathbb{K}_\sigma$$

$$\mathbb{M}_2 = \mathbb{L}_\sigma^t + \frac{1}{\Delta t}\mathbb{L}_\varepsilon, \quad \mathbb{M}_3 = \mathbb{G}_\sigma + \frac{1}{\Delta t}\mathbb{G}_\varepsilon$$

$$\mathbf{F}_{\mathbf{A}} = V_{\mathrm{s}}^{n+1}\mathbb{L}_\sigma \mathbf{X}_\alpha + \frac{V_{\mathrm{s}}^{n+1} - V_{\mathrm{s}}^n}{\Delta t}\mathbb{L}_\varepsilon \mathbf{X}_\alpha$$

$$\mathbf{F}_\varphi = V_{\mathrm{s}}^{n+1}\mathbb{G}_\sigma \mathbf{X}_\alpha + \frac{V_{\mathrm{s}}^{n+1} - V_{\mathrm{s}}^n}{\Delta t}\mathbb{G}_\varepsilon \mathbf{X}_\alpha$$

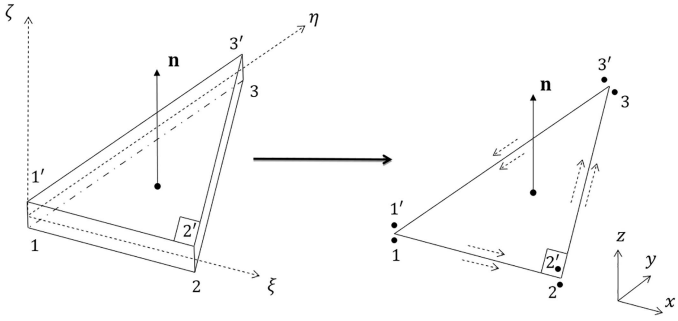

Fig. 2. Right triangular prism element (left) and the corresponding shell element (right).

where $\mathbf{X}_\alpha \in \mathbb{R}^{N_n}$ is the component vector of α, and

$$[\mathbb{M}_\nu]_{i,j} = \int_\Omega \nu \nabla \times \mathbf{w}_i^1 \cdot \nabla \times \mathbf{w}_j^1, \quad [\mathbb{K}_\sigma]_{i,j} = \int_{\Omega_c} \sigma \mathbf{w}_i^1 \cdot \mathbf{w}_j^1$$

$$[\mathbb{L}_\sigma]_{i,j} = \int_{\Omega_c} \sigma \nabla w_i^0 \cdot \mathbf{w}_j^1, \quad [\mathbb{L}_\varepsilon]_{i,j} = \int_\Omega \varepsilon \nabla w_i^0 \cdot \mathbf{w}_j^1$$

$$[\mathbb{G}_\sigma]_{i,j} = \int_{\Omega_c} \sigma \nabla w_i^0 \cdot \nabla w_j^0, \quad [\mathbb{G}_\varepsilon]_{i,j} = \int_\Omega \varepsilon \nabla w_i^0 \cdot \nabla w_j^0.$$

In the frequency domain, all the quantities depending on time are represented as being the real part of a complex quantity. In addition, the operator of the time derivative $\partial/\partial t$ becomes the factor $j\omega$, where ω is the angular frequency. Then, the complex system of the Darwin model is written as follows:

$$\begin{bmatrix} \mathbb{M}_\nu + j\omega\mathbb{K}_\sigma & \mathbb{L}_\sigma^t + j\omega\mathbb{L}_\varepsilon \\ \mathbb{L}_\sigma & \dfrac{1}{j\omega}\mathbb{G}_\sigma + \mathbb{G}_\varepsilon \end{bmatrix} \begin{bmatrix} \mathbf{X_A} \\ \mathbf{X}_\varphi \end{bmatrix} = - \begin{bmatrix} \mathbf{F_A}(\omega) \\ \mathbf{F}_\varphi(\omega) \end{bmatrix}. \tag{28}$$

Due to the removal of the rotational parts of the displacement current densities related to electromagnetic wave radiation, i.e., in the electric displacement currents, represented by $\varepsilon\partial^2\mathbf{A}/\partial t^2$ (or $\omega^2\varepsilon\mathbf{A}$) term, the resultant system matrix is no longer symmetric. Moreover, the matrix is ill-conditioned due to the high contrast of magnitudes of material coefficients [2]. In our study, the biconjugate gradient stabilized (BiCGSTAB) solver with a Split-Jacobi preconditioner [5] is used to solve the asymmetric systems (27) and (28).

V. Shell Elements

The shell element method consists in representing the thin structures by 2-D surfaces, separating two domains meshed with 3-D elements. Based on [12], the shell element is produced by the deformation of a prismatic element, as shown in Fig. 2. These deformed elements are built by doubling this surface mesh, i.e., both the nodes and the edges of the triangle. In other words, to obtain the shell element, the opposite nodes (1 and $1'$, 2 and $2'$, 3 and $3'$) are brought together to form a surface element where the nodes and the edges are duplicated but geometrically overlapping.

Let us recall that Ω is the study domain, which is decomposed into two regions: the Ω_s domain containing the 2-D meshed shell surfaces and Ω_{ns} which is the domain containing the 3-D meshed regions. We consider a right triangular prism having a thickness denoted by e and oriented in the ζ-direction, as illustrated on the left in Fig. 2. The bottom and top triangles are parallel and numerated by 123 and $1'2'3'$, respectively. The basic Whitney functions, for nodes and edges, for such an element are developed in the following.

A. Nodes Shape and Space Functions

The nodal interpolation functions of the reference element are written as follows:

$$w_i^0 = \lambda_i \beta \tag{29}$$

$$w_{i'}^0 = \lambda_i \beta' \quad \forall i = 1,2,3 \text{ and } i' = 1,'2,'3' \tag{30}$$

where λ_i are the coordinates of a point in a reference triangle defined by

$$\begin{cases} \lambda_1 = 1 - \xi - \eta \\ \lambda_2 = \xi \\ \lambda_3 = \eta \end{cases} \tag{31}$$

and $\beta = 1/2 - \zeta$ and $\beta' = 1/2 + \zeta$ are the linear interpolation functions along the ζ-axis with $0 \le \xi \le 1$, $0 \le \eta \le 1$, and $-1/2 \le \zeta \le 1/2$.

If W_t^0 is the set of nodal functions defined on a triangle, then the nodal prism functions can represent the union of the nodal triangular functions defined on the lower and upper side of the prism. We denote in the following by W_s^0 the set of the nodal prism functions [12], which can be represented by the nodal triangle element W_t^0 on the lower and upper surfaces of the prism:

$$\mathrm{W}_\mathrm{s}^0 = \left(\mathrm{W}_\mathrm{t}^0\beta, \mathrm{W}_\mathrm{t}^0\beta'\right). \tag{32}$$

1) Gradient in Reference Element: The gradient of W_s^0 reads as follows:

$$\nabla w_1^0 = \begin{pmatrix} -\beta \\ -\beta \\ -\lambda_1 \end{pmatrix} = \begin{pmatrix} \nabla_\mathrm{s} w_1^0 \beta \\ -\lambda_1 \end{pmatrix} \tag{33}$$

$$\nabla w_2^0 = \begin{pmatrix} \beta \\ 0 \\ -\lambda_2 \end{pmatrix} = \begin{pmatrix} \nabla_\mathrm{s} w_2^0 \beta \\ -\lambda_2 \end{pmatrix} \tag{34}$$

$$\nabla w_3^0 = \begin{pmatrix} 0 \\ \beta \\ -\lambda_3 \end{pmatrix} = \begin{pmatrix} \nabla_\mathrm{s} w_3^0 \beta \\ -\lambda_3 \end{pmatrix}. \tag{35}$$

In the same way, we obtain $\nabla w_{1'}^0$, $\nabla w_{2'}^0$, and $\nabla w_{3'}^0$ where $\nabla_\mathrm{s} w_{1^{(\prime)}}^0 = (-1,-1)$, $\nabla_\mathrm{s} w_{2^{(\prime)}}^0 = (1,0)$, and $\nabla_\mathrm{s} w_{3^{(\prime)}}^0 = (0,1)$ are the surface gradients in the triangular element.

2) Transformation Matrix: We define in the reference element the vertices $p_i(\xi_i, \eta_i, \zeta_i)$ and $p_{i'}(\xi_{i'}, \eta_{i'}, \zeta_{i'})$ $\forall i, i' = 1,2,3$, respectively. Let us take $p_1(0,0,-1/2)$, $p_2(1,0,-1/2)$, $p_3(0,1,-1/2)$, $p_{1'}(0,0,1/2)$, $p_{2'}(1,0,1/2)$, and $p_{3'}(0,1,1/2)$ the coordinates of the vertices of prism in the Cartesian reference system. For the real element, we define $\tilde{p}_i(x_i, y_i, z_i)$

and $\tilde{p}_{i'}(x_{i'}, y_{i'}, z_{i'})$ such as $\forall i = 1, 2, 3$ and $\forall i' = 1,' 2,' 3'$ with $i = i'$, we have

$$x_i = x_{i'}$$
$$y_i = y_{i'}$$
$$z_{i'} - z_i = e.$$

The real element can be defined as the image by a geometric transformation of a reference element for which the interpolation functions are known. The expressions of the elementary matrices show differential operators applied to the interpolation functions. However, in practice, we know the derivatives of the interpolation functions with respect to the coordinates of the reference element (ξ, η, ζ). It is, therefore, necessary to express the derivatives of the interpolation functions with respect to the real coordinates (x, y, z). Then, the transformation matrix is written as follows:

$$\begin{pmatrix} x \\ y \\ z \end{pmatrix} = \begin{pmatrix} x_2 - x_1 & x_3 - x_1 & 0 \\ y_2 - y_1 & y_3 - y_1 & 0 \\ 0 & 0 & e \end{pmatrix} \begin{pmatrix} \xi \\ \eta \\ \zeta \end{pmatrix} + \begin{pmatrix} x_1 \\ y_1 \\ z_1 + e/2 \end{pmatrix} = \mathbb{J} \begin{pmatrix} \xi \\ \eta \\ \zeta \end{pmatrix} + \begin{pmatrix} x_1 \\ y_1 \\ z_1 + e/2 \end{pmatrix} \tag{36}$$

where $\mathbb{J}$ is the Jacobian matrix of the transformation. By denoting that $\mathbb{J}_{\rm s} = \begin{pmatrix} x_2 - x_1 & x_3 - x_1 \\ y_2 - y_1 & y_3 - y_1 \end{pmatrix}$ is the Jacobian matrix for a triangular element, the Jacobian matrix $\mathbb{J}$ is written as follows:

$$\mathbb{J} = \left(\begin{array}{c|c} \mathbb{J}_{\rm s} & \mathbf{0} \\ \hline \mathbf{0} & e \end{array}\right). \tag{37}$$

3) Gradient in Real Element: By denoting $\tilde{w}^0$ a nodal function in the real coordinate system, one writes

$$\nabla \tilde{w}_i^0 = \mathbb{J}^{-t} \nabla w_i^0 \quad \forall i = 1, 2, 3. \tag{38}$$

For example, the gradient of $\tilde{w}_1^0$ is written as follows:

$$\nabla \tilde{w}_1^0 = \mathbb{J}^{-t} \nabla w_1^0 = \begin{pmatrix} \mathbb{J}_{\rm s}^{-t} \nabla_{\rm s} w_1^0 \beta \\ \hline \frac{-\lambda_1}{e} \end{pmatrix}. \tag{39}$$

In general, we write in the lower triangle element

$$\nabla \tilde{w}_i^0 = \begin{pmatrix} \mathbb{J}_{\rm s}^{-t} \nabla_{\rm s} w_1^0 \beta & \mathbb{J}_{\rm s}^{-t} \nabla_{\rm s} w_2^0 \beta & \mathbb{J}_{\rm s}^{-t} \nabla_{\rm s} w_3^0 \beta \\ \hline \frac{-\lambda_1}{e} & \frac{-\lambda_2}{e} & \frac{-\lambda_3}{e} \end{pmatrix}. \tag{40}$$

Similarly, in the upper triangle, we have

$$\nabla \tilde{w}_{i'}^0 = \begin{pmatrix} \mathbb{J}_{\rm s}^{-t} \nabla_{\rm s} w_1^0 \beta' & \mathbb{J}_{\rm s}^{-t} \nabla_{\rm s} w_2^0 \beta' & \mathbb{J}_{\rm s}^{-t} \nabla_{\rm s} w_3^0 \beta' \\ \hline \frac{\lambda_1}{e} & \frac{\lambda_2}{e} & \frac{\lambda_3}{e} \end{pmatrix}. \tag{41}$$

B. Edges Shape and Space Functions

The edge interpolation functions are defined by $\forall i, j = 1, 2, 3$ and $\forall i,' j' = 1,' 2,' 3'$

$$\mathbf{w}_{ij}^1 = (\lambda_i \nabla_{\rm s} \lambda_j - \lambda_j \nabla_{\rm s} \lambda_i) \beta \quad \forall i \neq j \tag{42}$$

$$\mathbf{w}_{i'j'}^1 = (\lambda_i \nabla_{\rm s} \lambda_j - \lambda_j \nabla_{\rm s} \lambda_i) \beta' \quad \forall i' \neq j' \tag{43}$$

$$\mathbf{w}_{ii'}^1 = \lambda_i (\beta' \nabla \beta - \beta \nabla \beta') \quad \forall i = i'. \tag{44}$$

Likewise, the shape functions of the edges defined on a triangle are the terms between the parenthesis of (42) and (43). Therefore, we denote in the following by $\mathbf{W}_{\rm s}^1$ the set of edge prism functions, which can be written as follows [12]:

$$\mathbf{W}_{\rm s}^1 = (\mathbf{W}_{\rm t}^1 \beta, \mathbf{W}_{\rm t}^1 \beta,' \mathrm{W}_{\rm t}^0 \mathbf{n}). \tag{45}$$

The third term of (45) is concluded from (44). In fact, since beta $\beta + \beta' = 1$ and $\nabla \beta = -\nabla \beta' = \mathbf{n}$, (44) can be simplified as

$$\mathbf{w}_{ii'}^1 = \lambda_i \mathbf{n}. \tag{46}$$

1) Rotational in Reference Element: In the following, an edge function and its rotational on the edge $p_1 p_2$, for example, are written as

$$\mathbf{w}_{12}^1 = \begin{pmatrix} (\lambda_1 + \lambda_2)\beta \\ \lambda_2 \beta \\ 0 \end{pmatrix} \quad \nabla \times \mathbf{w}_{12}^1 = \begin{pmatrix} \lambda_2 \\ \lambda_3 - 1 \\ 2\beta \end{pmatrix}. \tag{47}$$

Analogously, the other edge functions and their rotationals are computed.

2) Rotational in Real Element: By denoting $\tilde{\mathbf{w}}^1$ an edge function in the real coordinate system, one writes in the lower triangle

$$\tilde{\mathbf{w}}_{ij}^1 = \mathbb{J}^{-t} \mathbf{w}_{ij}^1 \quad \forall i \neq j \tag{48}$$

$$\nabla \times \tilde{\mathbf{w}}_{ij}^1 = \mathbb{J}^t \nabla \times \mathbf{w}_{ij}^1 \quad \forall i \neq j. \tag{49}$$

Then

$$\tilde{\mathbf{w}}_{ij}^1 = \begin{pmatrix} \mathbb{J}_{\rm s}^{-t} \mathbf{w}_{12}^1 \beta & \mathbb{J}_{\rm s}^{-t} \mathbf{w}_{13}^1 \beta & \mathbb{J}_{\rm s}^{-t} \mathbf{w}_{23}^1 \beta \\ 0 & 0 & 0 \end{pmatrix} \tag{50}$$

$$\nabla \times \tilde{\mathbf{w}}_{ij}^1 = \begin{pmatrix} \mathbb{J}_{\rm s}^t \nabla_{\rm s} \times \mathbf{w}_{12}^1 & \mathbb{J}_{\rm s}^t \nabla_{\rm s} \times \mathbf{w}_{13}^1 & \mathbb{J}_{\rm s}^t \nabla_{\rm s} \times \mathbf{w}_{23}^1 \\ 2\beta e & -2\beta e & 2\beta e \end{pmatrix}. \tag{51}$$

Similarly, in the upper triangle, we have

$$\tilde{\mathbf{w}}_{i'j'}^1 = \begin{pmatrix} \mathbb{J}_{\rm s}^{-t} \mathbf{w}_{1'2'}^1 \beta' & \mathbb{J}_{\rm s}^{-t} \mathbf{w}_{1'3'}^1 \beta' & \mathbb{J}_{\rm s}^{-t} \mathbf{w}_{2'3'}^1 \beta' \\ 0 & 0 & 0 \end{pmatrix} \tag{52}$$

$$\nabla \times \tilde{\mathbf{w}}_{i'j'}^1 = \begin{pmatrix} \mathbb{J}_{\rm s}^t \nabla_{\rm s} \times \mathbf{w}_{1'2'}^1 & \mathbb{J}_{\rm s}^t \nabla_{\rm s} \times \mathbf{w}_{1'3'}^1 & \mathbb{J}_{\rm s}^t \nabla_{\rm s} \times \mathbf{w}_{2'3'}^1 \\ 2\beta' e & -2\beta' e & 2\beta' e \end{pmatrix}. \tag{53}$$

It should be mentioned here that the prism collapsed into a triangular element while retaining the total number of DoF associated with the prism, as shown in Fig. 2. In addition, the normal edges might not be taken into account that may correspond to a partial gauge imposed on the vector potential $\mathbf{A}$.

C. Shell Elements Hypothesis

Considering that a thin structure has a small thickness e, the main idea of this method is to avoid the meshing of the thin structures by modeling them on surfaces without thickness. The

shell element is obtained by degenerating a prismatic element into two superimposed triangles, as shown in Fig. 2. Indeed, the thin structure is modeled in 2-D and meshed by triangular elements where both nodes and edges will be duplicated on the surfaces. In addition, the track thickness e is taken into account in the volume integral of the variational formulation. These integrals are decomposed into surface integrals obtained by the Gaussian quadrature method and an analytical integral computed along the z-axis.

D. Approximation of φ and $\mathbf{A}$

According to the previous assumptions, the ESP φ and the MVP $\mathbf{A}$, as well as their gradient and their rotational, are approximated by the nodal and edge functions of the shell elements, respectively.

In the shell region, φ is discretized in each shell element by the nodal interpolation function as follows:

$$\varphi = \sum_{i=1}^{N_n} \varphi_i \tilde{w}_i^0 + \sum_{i'=1}^{N_n} \varphi_{i'} \tilde{w}_{i'}^0. \tag{54}$$

Then, the gradient of φ reads

$$\nabla\varphi = \sum_{i=1}^{N_n} \varphi_i \nabla\tilde{w}_i^0 + \sum_{i'=1}^{N_n} \varphi_{i'} \nabla\tilde{w}_i^0 \tag{55}$$

where N_n is the cardinal of the set of nodes of the triangular element. In addition, $\mathbf{A}$ is discretized in each shell element by the edge interpolation function as follows:

$$\mathbf{A} = \sum_{i,j=1}^{N_e} A_i \tilde{\mathbf{w}}_{ij}^1 + \sum_{i,'j'=1}^{N_e} A_{i'} \tilde{\mathbf{w}}_{i'j}^1 \tag{56}$$

with $A_{1^{(\prime)}}$, $A_{2^{(\prime)}}$, $A_{3^{(\prime)}}$ the circulation of $\mathbf{A}$ along the edges defined by the nodes $1^{(\prime)}$ and $2^{(\prime)}$, $2^{(\prime)}$ and $3^{(\prime)}$, and $3^{(\prime)}$ and $1^{(\prime)}$, respectively. Then, the rotational of $\mathbf{A}$ will be expressed as

$$\nabla \times \mathbf{A} = \sum_{i,j=1}^{N_e} A_i \nabla \times \tilde{\mathbf{w}}_{ij}^1 + \sum_{i,'j'=1}^{N_e} A_{i'} \nabla \times \tilde{\mathbf{w}}_{i'j'}^1 \tag{57}$$

where N_e is the cardinal of the set of edges of the triangular element.

The approximations defined above allow a natural continuity of the variables on the interfaces of the thin shell and the various neighboring domains.

VI. Applications

The validation of the implementation of the Darwin model combined with the shell elements is presented in time domain in Appendix A for an academic test case.

In this section, two different examples of PCBs are carried out: a single-sided PCB and a double-sided one. For the first example, the global and local results obtained by the numerical simulation are presented as well as a comparison with measurements is provided. For the second one, the interest is to show the coupling of 2-D and 3-D domains in conductivity and to model the capacitive–inductive effects in the intermediate frequency range, in particular, for frequencies close to the resonant frequency. The numerical simulation results for the two considered PCBs are obtained by applying the Darwin model in both time domain (27) and frequency domain (28). More information about the two PCB examples can be found in [25].

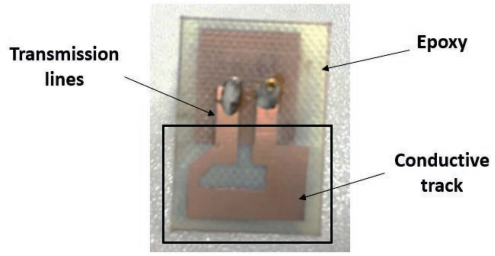

Fig. 3. Real device of the single-sided PCB.

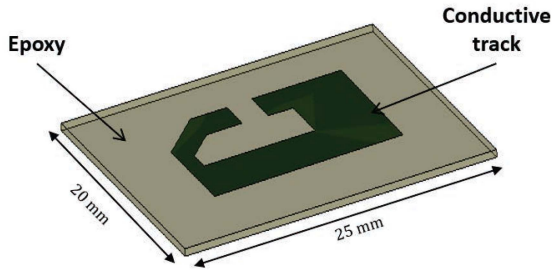

Fig. 4. PCB model.

A. Single-Sided PCB

A single-sided PCB, as shown in Fig. 3, is considered to study their behavior and to validate the implementation of the combination of the shell element method and the Darwin model by resorting to the measurements. The simulation results are presented both for the local field distributions and the global quantity as the impedance in the frequency domain and for the total transient current in the time domain.

For this example, the PCB framed in the black box is modeled, as shown in Fig. 3, where the transmission lines are not taken into account. The PCB model is composed of a copper loop conductor, as shown in green in Fig. 4, having a thickness of $35\mu\mathrm{m}$ and modeled in 2-D in order to apply the shell elements. The conductor is placed on an epoxy layer having a height of 0.4 mm.

Three different domains are considered: copper, epoxy, and the air box. The electric conductivity of the conductor (green part) is taken as 59.6 MS/m. The relative permittivity of the conductor is set to 1 and 4.4 for the dielectric epoxy (gray part), while the relative permeability is set as 1 in all domains.

For the computational configurations, a fixed potential V_s is applied to a terminal of the conductor with $V_{\mathrm{s}_{\max}} = 1\,\mathrm{mV}$, marked in red in Fig. 5, of the conductive track using the wheelbase of the 1206 capacitor.[1]

[1][Online]. Available: https://www.mouser.com/catalog/supplier/library/avxshortform.pdf

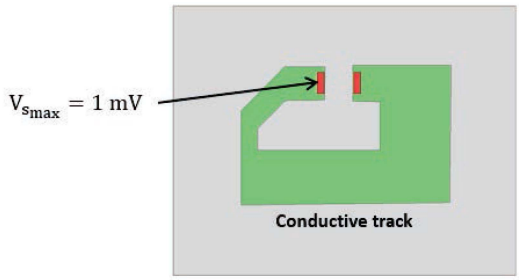

Fig. 5. Imposed voltage sections.

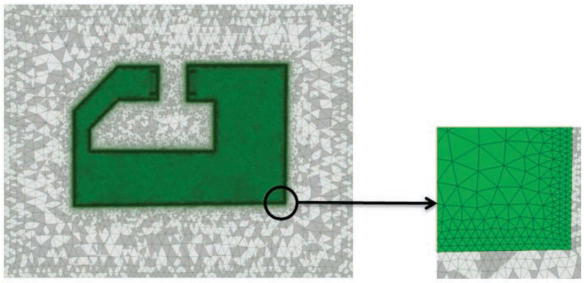

Fig. 6. Considered mesh.

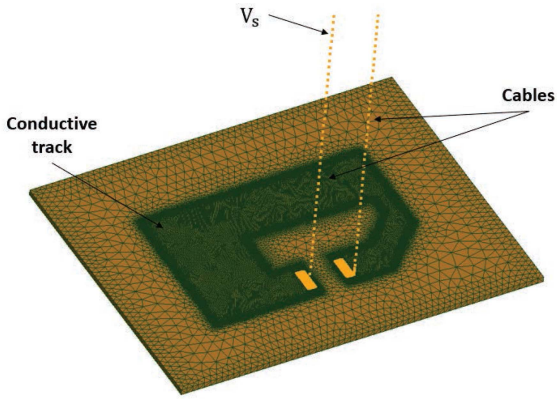

Fig. 7. PCB connections with two electric cables.

Considering the skin effect when the frequency increases, the used mesh features 2 092 863 tetrahedrons in the 3-D domains and 86 970 triangles in the 2-D conductive track. The mesh of the geometry is presented in Fig. 6.

Two perfect 1-D electric cables are connected to the conductive track touching the air box in order to impose an ESP, as shown in Fig. 7. The boundary condition as $\mathbf{E} \times \mathbf{n} = \mathbf{0}$ $(\mathbf{B} \cdot \mathbf{n} = 0)$ is imposed on these cables.

1) Frequency Study: In this part, we study the single-sided PCB model in the frequency domain where the frequency interval is fixed as $[1 : 10^6]$ Hz in order to validate the integration of the shell elements in our software *code_Carmel* [26]. The computational time takes about 1.4 h for approximately 3 M DoFs using the BiCGSTAB solver for one frequency.

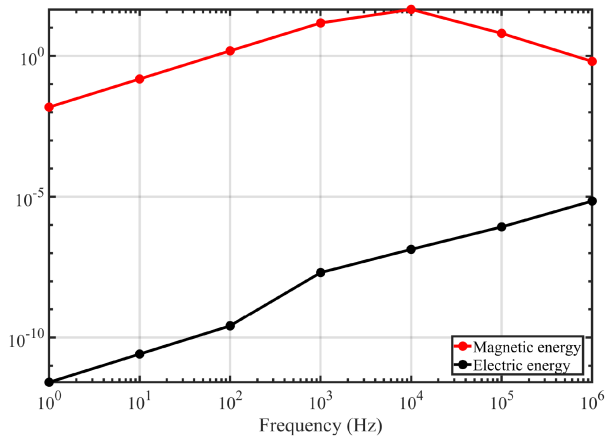

Fig. 8. Magnetic and electrical energies (J) computed versus frequency.

a) Computation of energies: In this part, we compute the magnetic and electrical energies in order to show that the capacitance is neglected in the considered frequency range. Based on the power balance S, we have

$$\underline{S} = j\omega W_{\mathrm{m}} + j\omega W_{\mathrm{e}} + P_{\mathrm{j}} \tag{58}$$

$$= \underline{V}\,\underline{I}^{*} \tag{59}$$

where $\underline{S}$, $\underline{V}$, and $\underline{I}^{*}$ represent the apparent power, the complex voltage, and the complex current conjugate, respectively. Additionally, W_{m}, W_{e}, and P_{j} represent the magnetic energy, the electrical energy, and the Joule losses, respectively. Indeed, in Fig. 8, the curves of the first two terms of (58) are presented. It can be observed that the magnetic energy is dominant and the electrical one is negligible in the fixed frequency interval.

b) Computation of PCB inductance: To compute the PCB inductance, we should first know the cable inductances. The global magnetic inductance $\mathrm{L_g}$ of the system is written as follows:

$$\mathrm{L_g} = \mathrm{L_{pcb}} + \mathrm{L_c} \tag{60}$$

where $\mathrm{L_{pcb}}$ and $\mathrm{L_c}$ are the inductance of the PCB and the cable, respectively.

The magnetic inductance is computed in the linear case as a function of the magnetic energy W_{m} with

$$W_{\mathrm{m}} = \frac{1}{2}\int_{\Omega} \mathbf{B} \cdot \mathbf{H}\, d\Omega = \frac{1}{2} L |\underline{I}|^2. \tag{61}$$

In order to compute the inductance of cables, another geometry is considered by reducing the size of the cables three times compared to the initial geometry. We keep the same mesh assumptions for the two geometries. Then, we obtain the first equation

$$\mathrm{L_c} = 3\mathrm{L_c'} \tag{62}$$

where $\mathrm{L_c'}$ is the inductance of the cables of the second geometry.

For the first geometry, the length of the cables is set to 75 mm, we had a global inductance of $\mathrm{L_g} = 128$ nH. For the second one, the cables length is fixed at 25 mm; therefore, the new inductance is equal to $\mathrm{L_g'} = 52.6$ nH.

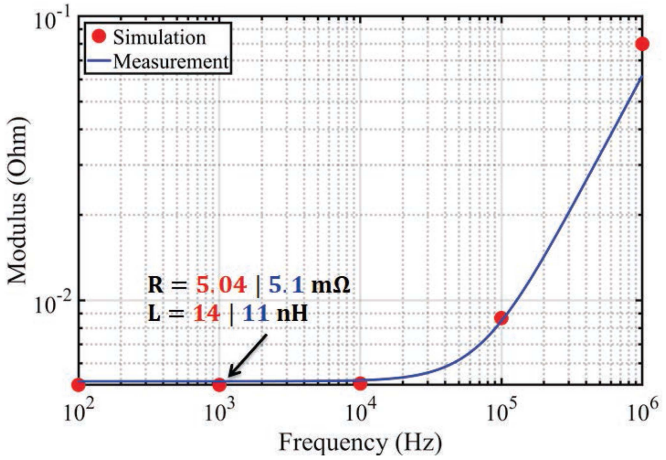

Fig. 9. Modulus of impedance versus frequency.

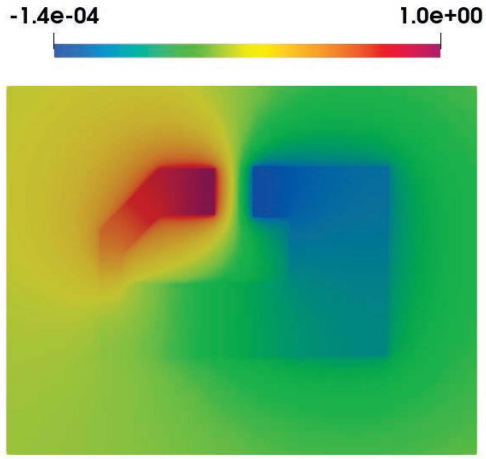

Fig. 10. Distribution of the scalar electric potential (V) in the whole domain.

Since the inductance of the PCB remains constant for both cases, a system of equations with three unknowns can be written as follows:

$$\begin{cases} \mathrm{L_g} = \mathrm{L_{pcb}} + \mathrm{L_c} \\ \mathrm{L'_g} = \mathrm{L_{pcb}} + \mathrm{L'_c} \end{cases}.$$

Then, by subtracting the two equations, we obtain

$$\mathrm{L_c} - \mathrm{L'_c} = 75.4\,\mathrm{nH}. \tag{63}$$

By (62) and (63), we get the cable inductance $\mathrm{L_c} = 111.75\,\mathrm{nH}$. Therefore, the inductance of PCB is $\mathrm{L_{pcb}} = 13.9\,\mathrm{nH}$ for $f = 1$ Hz.

c) Measurement and simulation comparison: Experimentally, the inductance value of the PCB is 11 nH indicating that the value obtained by the numerical simulation is close. It should be mentioned here that we present the results of the inductance for a single frequency since it is constant in our considered frequency interval.

In Fig. 9, the evolution of the modulus of the impedance as a function of the frequency obtained from the Darwin model and measurements is presented.

In low frequencies, the impedance Z corresponds to the dc resistance of the track. We obtain $Z = R_{\mathrm{DC}} = 5.04\,\mathrm{m\Omega}$ with the numerical simulation while $R = 5.1\,\mathrm{m\Omega}$ is obtained by the measurements, which shows a good agreement. In the interval $[10^2 : 10^4]$ Hz, the effects are decoupled such that the resistance can be acquired by the electrokinetic problem and the inductance by the magnetostatic one. When the frequency increases, the resistance also increases since the skin effect appears in the conductive track. For $f > 10$ kHz, the evolution of the impedance computed by the Darwin model presents the coupled resistive–inductive phenomena, which increase similarly to the measurements and with close values.

d) Electric potential and current density distributions: In Fig. 10, the distribution of the ESP is presented. We notice a linear decrease taking place along the track in a normal way starting from the maximum value of the excitation voltage $V_{\mathrm{s_{max}}} = 1$ V for $f = 1$ Hz.

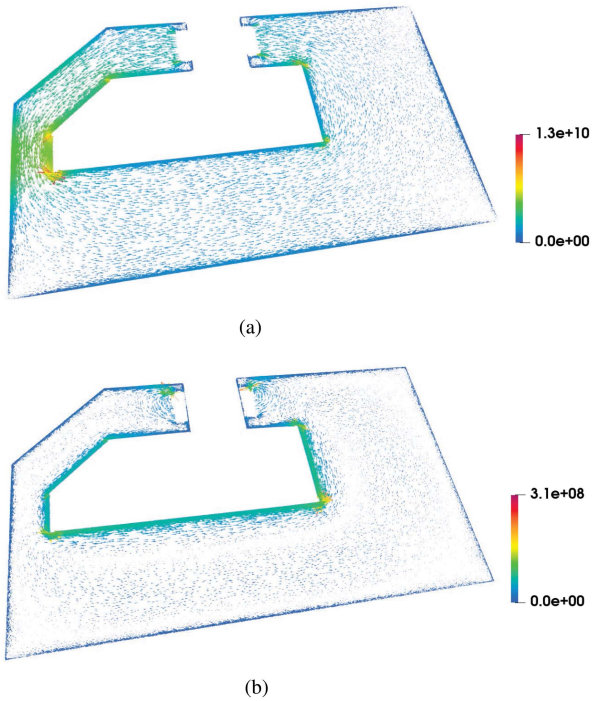

Fig. 11. Distribution of the current density $\mathbf{J}(\mathrm{A.m^{-2}})$ in the track for different frequencies. (a) $f = 1$ Hz. (b) $f = 100$ kHz.

In Fig. 11, the current density distribution is shown for two different frequencies. The magnitude of the current density for $f = 1$ Hz is illustrated in Fig. 11(a), where the distribution is only influenced by the geometry of the track. On the other hand, for $f = 100$ kHz shown in Fig. 11(b), the amplitude of the current density is restricted to a small layer at the outskirts of the track due to the skin effect.

2) Time Study: In this part, we study the same example in the time domain in order to present the evolution of the current flowing out the terminal of the conductive track.

A pulse voltage source in the form of a square wave is applied between the terminals with $V_{\mathrm{s_{max}}} = 1$ at the frequency of

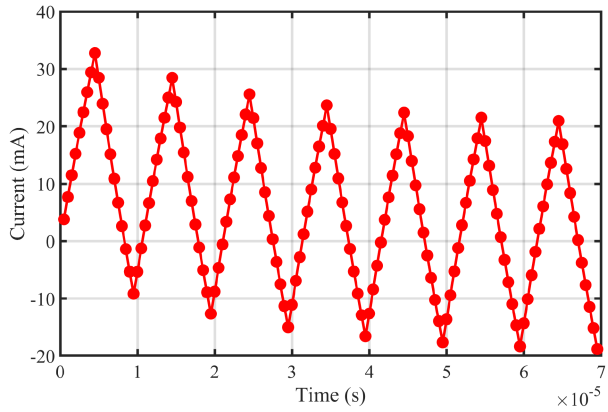

Fig. 12. Evolution of the current (mA) when the frequency of the excitation is $f = 100$ kHz.

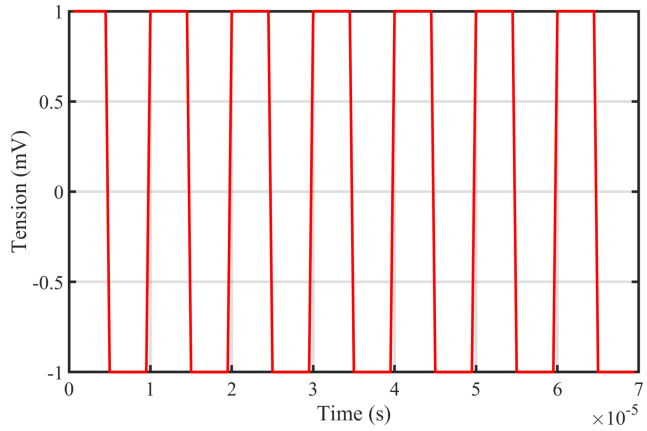

Fig. 13. Voltage source (mV) (square wave).

$f = 100$ kHz. By considering the same mesh shown in Fig. 6, the BiCGSTAB is used with a Split-Jacobi preconditioner to solve the Darwin formulation in the time domain. Then, Fig. 12 gives the transient state of the current in the first seven periods when the voltage source is a square wave, as shown in Fig. 13. The computation time for one-time step takes around 40 min.

B. Double-Sided PCB

In this example, the 3-D/2-D coupling of the different conductive domains and the coupled capacitive-inductive effects when the frequency increases are presented. The real device of the double-sided PCB is shown in Fig. 14.

Analogously to the first PCB example, only the copper part is modeled, framed in the black box as shown in Fig. 14, while the transmission lines are not taken into account. The PCB model is composed of three copper conductive tracks, two on the top side and one on the bottom, as shown in green in Fig. 15, having a thickness of 35 μm. The two sides are connected by hollow conductive via modeled in 3-D with a cylindrical shape having a thickness of 20 μm. The two sides are separated by the epoxy having a height of 0.4 mm.

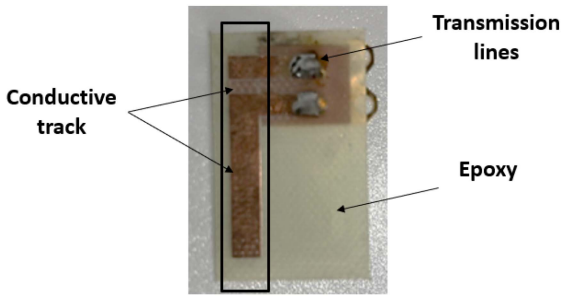

Fig. 14. Real device of the double-sided PCB.

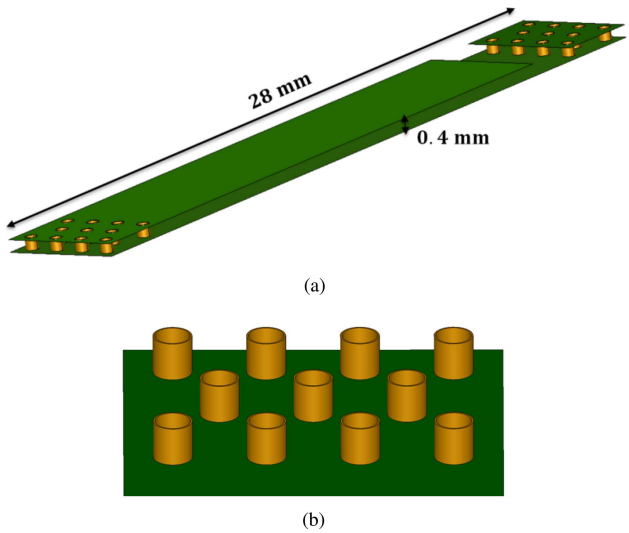

Fig. 15. Considered model. (a) PCB model. (b) 3-D conductive via.

Fig. 16. Imposed voltage sections.

The double-sided example is made up of four different domains. The 2-D and 3-D conductive domains are made of copper, and the epoxy is an insulator that separates the conductive tracks and the air box. The characteristics of the materials are the same as defined in the previous application.

For the computational configurations, a fixed potential V_s is applied to a terminal of the conductor (red part) using the wheelbase of the 1206 capacitor, as shown in Fig. 16, and touching the air box via 1-D perfect electric cables. The mesh used for the model features 2 053 918 3-D tetrahedral elements and 125 914 2-D triangular elements in the tracks. The mesh of the geometry is presented in Fig. 17.

1) Frequency Study: For the frequency computation, the frequency interval is fixed as $[1 : 10^{11}]$ Hz in order to illustrate

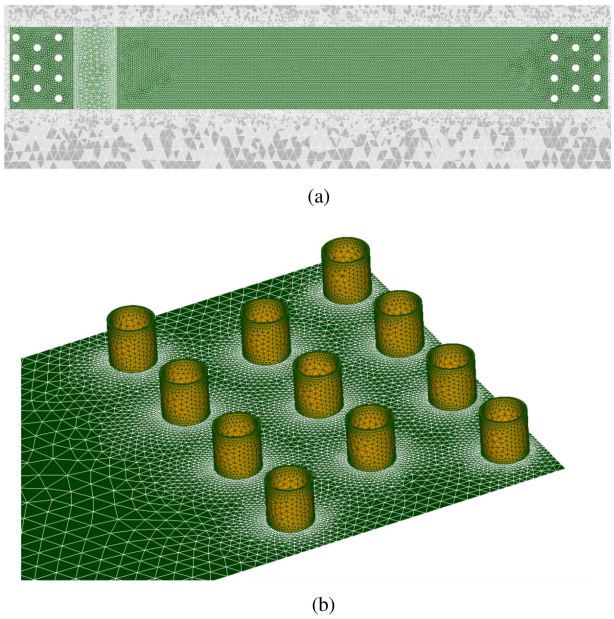

(a)

(b)

Fig. 17. Considered mesh. (a) Mesh for whole domain (top view). (b) Mesh in the conductive via.

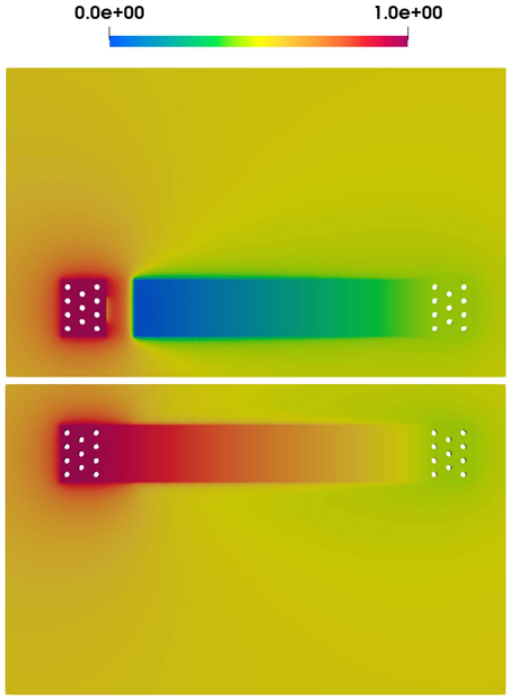

Fig. 18. Distribution of the scalar electric potential (V) in the whole domain for $f = 1$ Hz.

the capacitive–inductive coupled effects when the frequency increases. The resonant frequency is presented for this example by computing the impedance versus the frequency. The computational time takes about 1.3 h for 2 745 802 DoFs by applying the Darwin model using the BiCGSTAB solver for one frequency.

a) Electric potential and current density distributions: The electromagnetic fields are presented for different frequencies where the 3-D/2-D coupling between the different domains of the application is clearly shown. On the one hand, the distribution of the ESP in the whole domain is presented in Fig. 18. A linear decrease can be observed in the distribution of the electric potential. Besides, the electric potential is well recovered on the bottom side of the track by the conductive via. On the other hand, the distribution of the current density is presented for two frequencies in the tracks and the conductive via, as shown in Fig. 19.

b) Electric field between the two tracks: The electric field is presented in Fig. 20 between the 2-D conductive tracks for different frequencies in order to show the resonant effects in a section of the epoxy. Before the resonant frequency, the electric field is distributed in the same direction, as can be seen in Fig. 20(a) and (b). Besides, the resonance effect can be observed in Fig. 20(c) for $f = 1$ GHz. Therefore, the electric field is distributed in two opposite directions.

c) Evolution of the impedance versus the frequency: The evolution of the modulus of the impedance as a function of the frequency is presented in Fig. 21. The measurements are not provided for this example. However, the capacitive–inductive coupled effects when the frequency increases can be illustrated.

At low frequencies, the electromagnetic effects are decoupled, which shows the resistive effect until 1 kHz. When the frequency increases, the skin effect appears in the conductor, then the value

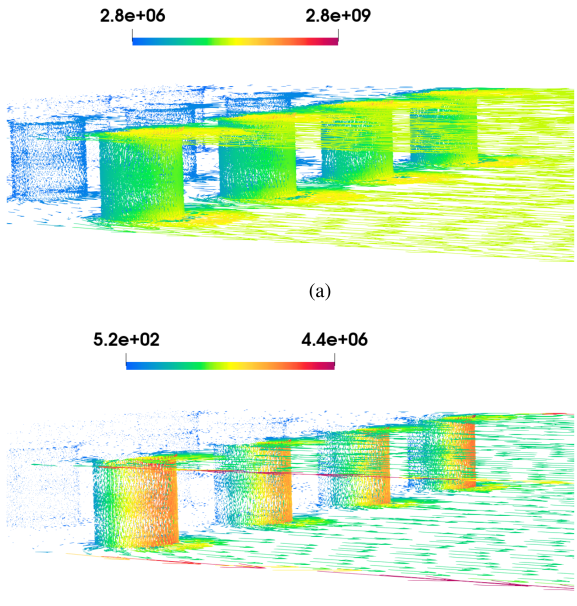

(a)

(b)

Fig. 19. Distribution of the current density $\mathbf{J}(\mathrm{A.m^{-2}})$ in the tracks and the conductive via. (a) $f = 10$ kHz. (b) $f = 10$ MHz.

of the resistance of the conductor increases. In particular, in the interval $[10^3 : 2 \times 10^8]$ Hz, the resistive–inductive effects are coupled. This zone corresponds to an eddy-current problem. For $f > 200$ MHz, the influence of the capacitive effects appears on the evolution of the impedance where the resonant frequency is around 300 MHz.

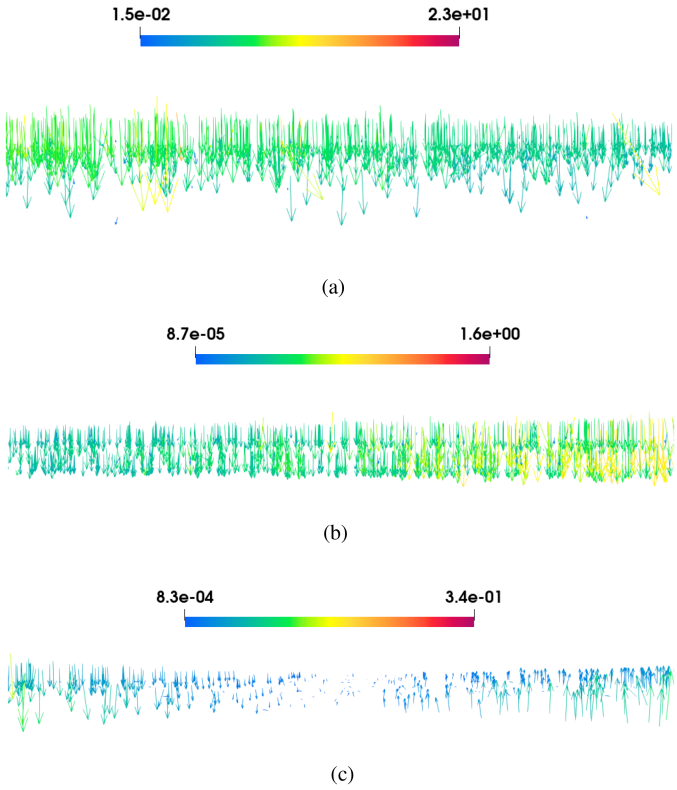

Fig. 20. Distribution of the electric field $\mathbf{E}(\mathrm{V/m})$ between the tracks with different frequencies. (a) $f = 1$ MHz. (b) $f = 100$ MHz. (c) $f = 1$ GHz.

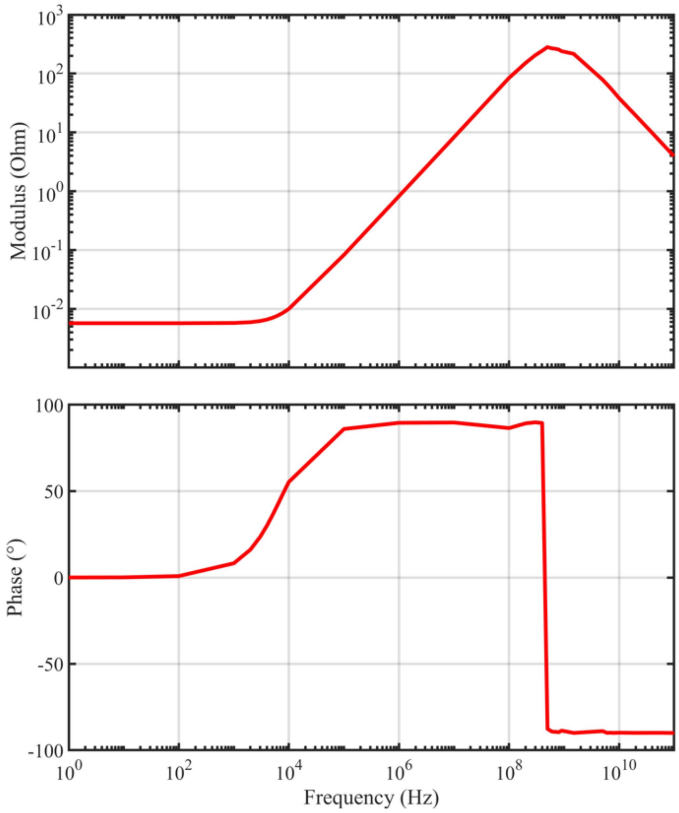

Fig. 21. Modulus of the impedance and phase versus frequency.

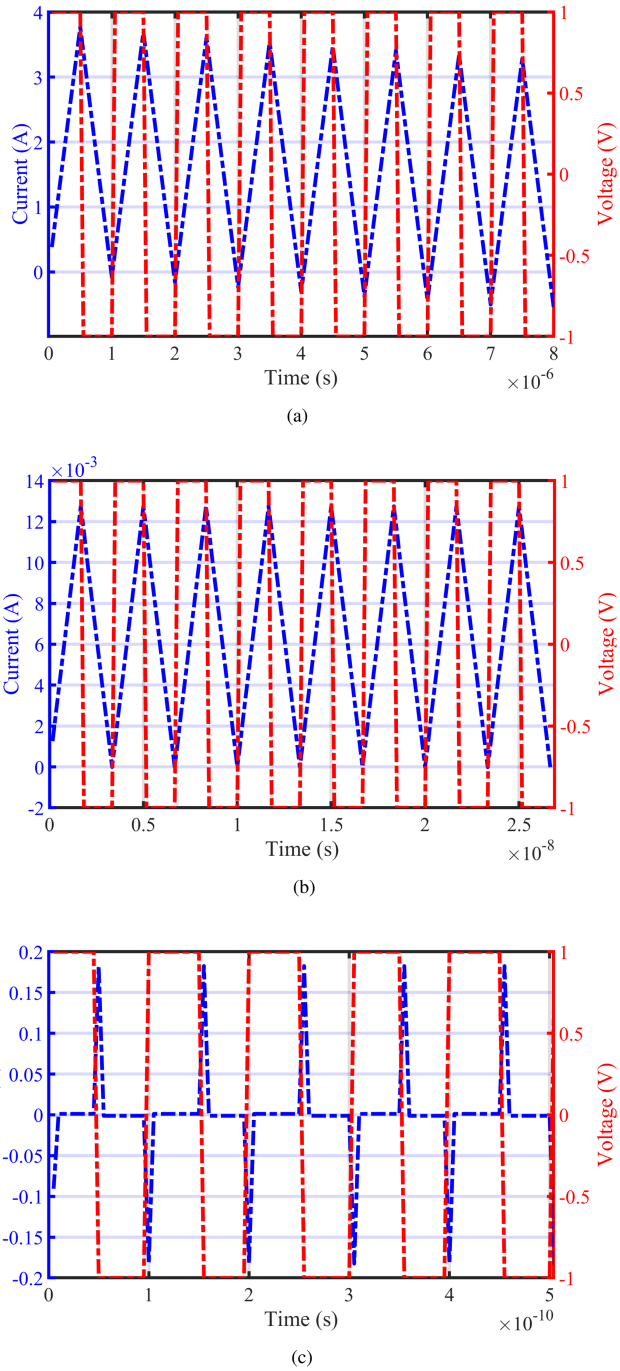

Fig. 22. Evolution of the current (A) for different frequencies. (a) $f = 1$ MHz. (b) $f = 300$ MHz. (c) $f = 10$ GHz.

2) Time Study: In this part, we study the same example in the time domain in order to present the evolution of the current flowing out the terminal of the conductive track for different frequencies of excitations, in particular, before, around, and after the resonant frequency.

A pulse voltage source in the form of a square wave is applied between the terminals with $V_{\mathrm{s_{max}}} = 1$ at $f = 1$ MHz, $f = 300$ MHz, and $f = 10$ GHz. The computation time for one-time step takes around 0.8 h. Before the resonant frequency,

for $f = 1$ MHz, a transient state of the current in the first eight periods when the voltage source is a square wave can be observed, as shown in Fig. 22(a). The circuit is represented by a series RL regime where the capacitive effects are still negligible. However, for $f = 300$ MHz, as the modulus of Z reaches its maximum, the magnitude of the current decreases with a transient state more significant in the first eight periods, as shown in Fig. 22(b). Besides, after the resonant frequency, the capacitive effects become dominant, and consequently, a significant current flows through the capacitors, representing a parallel RC regime, as shown in Fig. 22(c).

VII. Conclusion

The Darwin model is solved by integrating the shell element method, applied to both node and edge elements, in order to reduce the number of elements in the mesh and, consequently, the computational cost and time. To validate the practical formulation, two cases have been considered and studied in both time and frequency domains. The first case consisted in comparing the computed impedances of a single-sided PCB against measurements on a real device where the results show a good agreement. The second one consisted in modeling the resistive, inductive, and capacitive effects and the 3-D/2-D coupling of the conductive domains. In our further work, we will model PCBs with more complex structures as well as we will take into account the passive components such as inductors, capacitors, and resistors.

Appendix

A. Numerical Validation of Shell Elements

We present the results of the comparison obtained by different meshes for a simple test case composed of a conductor in L shape enclosed by an air box, as shown in Fig. 23, in order to validate the implementation of shell elements.

Two different domains are considered: a conductor in L shape and an air box. The electric conductivity of the conductor (green part) is taken as 1 MS/m. The relative permeability and permittivity are set to 1 in all domains.

1) Computational Configurations: The thickness of the conductor is fixed at 1.05 mm. Since the shell elements studied in this work are derived from the degeneration of prismatic elements, the conductor is spatially discretized in 3-D with prismatic elements composed of 3152 elements, as shown in Fig. 24(a), as well as pyramid and tetrahedral elements in the air box composed of 140 and 55 928 elements, respectively. On the other hand, for the second mesh, the 2-D conductor is discretized by 3152 triangular elements, as shown in Fig. 24(b), and 53 957 tetrahedral elements in the air.

Since the model is solved by the Darwin formulation, the unknowns of the system are defined on the nodes and the edges. The numbers of DoFs of φ and $\mathbf{A}$ are 11 402 and 71 197 for the first mesh, while they are equal to 11 063 and 67 529 for the second one. Note that the difference existing in the number of DoFs is due to the mesh of the air box, which is not exactly the same for the two cases.

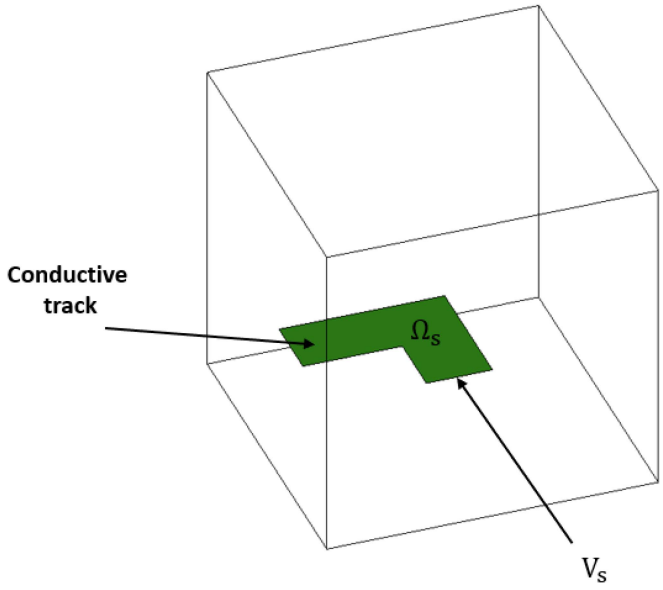

Fig. 23. Studied domain.

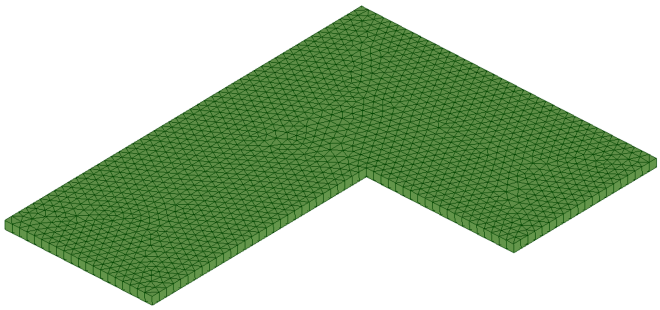

(a)

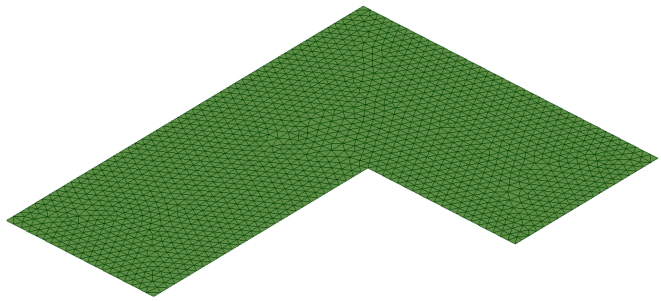

(b)

Fig. 24. Considered meshes. (a) 3-D mesh. (b) 2-D mesh.

The boundary condition Γ_{E} is imposed on the terminals of the conductor. A sinusoidal fixed potential V_{s} is applied to a terminal of the conductor with $V_{\mathrm{s}_{\max}} = 1$ mV for a frequency $f = 100$ kHz.

For each time step, the computational time, using the preconditioned BiCGSTAB solver, takes about 8 s for the first case while it takes 7.8 s for the second one.

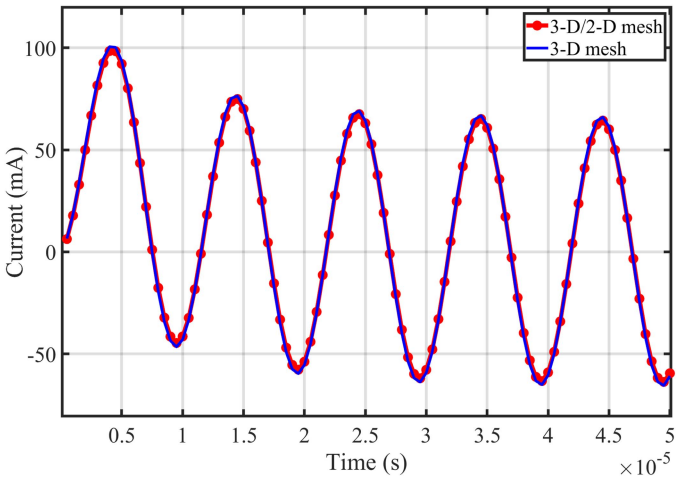

Fig. 25. Evolution of the current (mA) when the frequency of the excitation is $f = 100$ kHz.

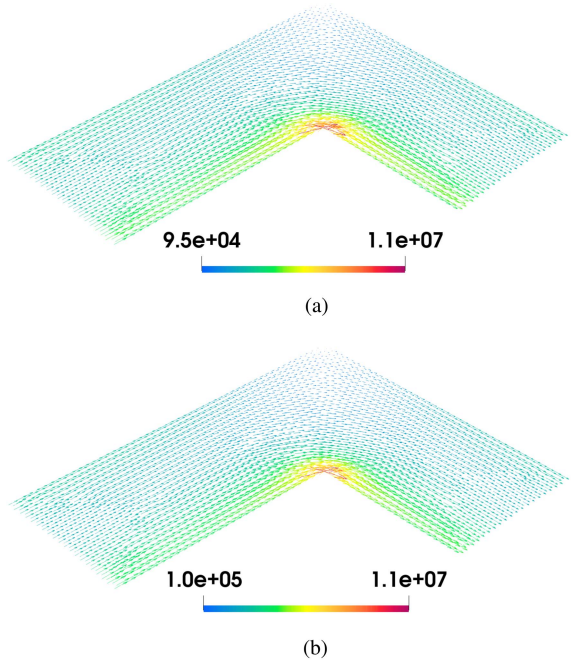

Fig. 26. Distribution of the current density $\mathbf{J}(\mathrm{mA.m^{-2}})$ in the conductor at $t = 35\,\mu$s. (a) 3-D mesh. (b) 2-D mesh.

2) Evolution of the Global Current: The evolution of the transient currents for the first five periods is presented for the two cases in Fig. 25. We can see in Fig. 25 that the results obtained with both meshes are very similar. Then, the current is well computed by the shell elements.

3) Electric and Magnetic Fields in the Track: In this section, we compare the current density $\mathbf{J}$ and the magnetic flux density $\mathbf{B}$ distributions in the conductor obtained by the two meshes, as shown in Fig. 26 and Fig. 27. The distribution of $\mathbf{J}$ is presented in Fig. 26(a) for the 3-D conductor while it is presented in Fig. 26(b) for the 2-D one. A good current distribution is obtained in the 2-D conductor as well as a good agreement with the result obtained for the 3-D conductor can be observed at the magnitude level.

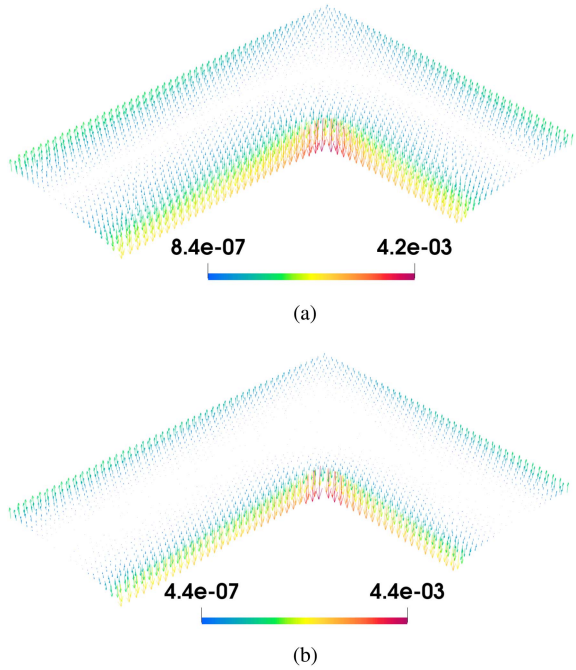

Fig. 27. Distribution of the magnetic flux density $\mathbf{B}$ (mT) in the conductor at $t = 35\,\mu$s. (a) 3-D mesh. (b) 2-D mesh.

Likewise, regarding the magnetic flux density distribution, it can be observed that the distribution in the 3-D conductor [see Fig. 27(a)] is very close to that obtained for the 2-D one [see Fig. 27(b)].

REFERENCES

[1] J. Larsson, "Electromagnetics from a quasistatic perspective," *Am. J. Phys.*, vol. 75, no. 3, pp. 230–239, Jul. 2007.
[2] S. Koch, H. Schneider, and T. Weiland, "A low-frequency approximation to the Maxwell equations simultaneously considering inductive and capacitive phenomena," *IEEE Trans. Magn.*, vol. 48, no. 2, pp. 511–514, Feb. 2012.
[3] Y. Zhao and Z. Tang, "A novel gauged potential formulation for 3-D electromagnetic field analysis including both inductive and capacitive effects," *IEEE Trans. Magn.*, vol. 55, no. 6, Jun. 2019, Art. no. 7400905.
[4] M. Clemens, B. Kähne, and S. Schöps, "A Darwin time domain scheme for the simulation of transient quasistatic electromagnetic fields including resistive, capacitive and inductive effects," in *Proc. Kleinheubach Conf.*, 2019, pp. 1–4.
[5] H. Taha, Z. Tang, T. Henneron, Y. Le Menach, F. Salomez, and J.-P. Ducreux, "Numerical simulation-based investigation of the limits of different quasistatic models," *Appl. Sci.*, vol. 11, no. 23, 2021, Art. no. 11218.
[6] D. Rodger, N. Atkinson, and P. Leonard, "Transient 3D eddy currents in thin sheet conductors," *IEEE Trans. Magn.*, vol. 24, no. 6, pp. 2691–2693, Nov. 1988.
[7] L. Krahenbuhl and D. Muller, "Thin layers in electrical engineering-example of shell models in analysing eddy-currents by boundary and finite element methods," *IEEE Trans. Magn.*, vol. 29, no. 2, pp. 1450–1455, Mar. 1993.
[8] I. Mayergoyz and G. Bedrosian, "On calculation of 3-D eddy currents in conducting and magnetic shells," *IEEE Trans. Magn.*, vol. 31, no. 3, pp. 1319–1324, May 1995.

[9] C. Guerin, G. Tanneau, G. Meunier, X. Brunotte, and J.-B. Albertini, "Three dimensional magnetostatic finite elements for gaps and iron shells using magnetic scalar potentials," *IEEE Trans. Magn.*, vol. 30, no. 5, pp. 2885–2888, Sep. 1994.

[10] J. Pavo, "Approximate methods for the calculation of the ECT signal of a crack in a plate coated by conducting deposit," *IEEE Trans. Magn.*, vol. 40, no. 2, pp. 659–662, Mar. 2004.

[11] O. Biro, I. Bardi, K. Preis, W. Renhart, and K. Richter, "A finite element formulation for eddy current carrying ferromagnetic thin sheets," *IEEE Trans. Magn.*, vol. 33, no. 2, pp. 1173–1178, Mar. 1997.

[12] Z. Ren, "Degenerated Whitney prism elements-general nodal and edge shell elements for field computation in thin structures," *IEEE Trans. Magn.*, vol. 34, no. 5, pp. 2547–2550, Sep. 1998.

[13] C. Geuzaine, P. Dular, and W. Legros, "Dual formulations for the modeling of thin electromagnetic shells using edge elements," *IEEE Trans. Magn.*, vol. 36, no. 4, pp. 799–803, Jul. 2000.

[14] Y. Choua, L. Santandrea, Y. Le Bihan, and C. Marchand, "Thin crack modeling in ECT with combined potential formulations," *IEEE Trans. Magn.*, vol. 43, no. 4, pp. 1789–1792, Apr. 2007.

[15] A. Ruehli, "Equivalent circuit models for three-dimensional multiconductor systems," *IEEE Trans. Microw. Theory Techn.*, vol. 22, no. 3, pp. 216–221, Mar. 1974.

[16] D. Gope, A. Ruehli, C. Yang, and V. Jandhyala, "(S)PEEC: Time- and frequency-domain surface formulation for modeling conductors and dielectrics in combined circuit electromagnetic simulations," *IEEE Trans. Microw. Theory Techn.*, vol. 54, no. 6, pp. 2453–2464, Jun. 2006.

[17] G. Antonini and D. Romano, "Efficient frequency-domain analysis of PEEC circuits through multiscale compressed decomposition," *IEEE Trans. Electromagn. Compat.*, vol. 56, no. 2, pp. 454–465, Apr. 2014.

[18] F. Ferranti, M. S. Nakhla, G. Antonini, T. Dhaene, L. Knockaert, and A. E. Ruehli, "Multipoint full-wave model order reduction for delayed PEEC models with large delays," *IEEE Trans. Electromagn. Compat.*, vol. 53, no. 4, pp. 959–967, Nov. 2011.

[19] R. Torchio, F. Moro, G. Meunier, J.-M. Guichon, and O. Chadebec, "An extension of unstructured-PEEC method to magnetic media," *IEEE Trans. Magn.*, vol. 55, no. 6, Jun. 2019, Art. no. 7200404.

[20] J. Siau, G. Meunier, O. Chadebec, J.-M. Guichon, and R. Perrin-Bit, "Volume integral formulation using face elements for electromagnetic problem considering conductors and dielectrics," *IEEE Trans. Electromagn. Compat.*, vol. 58, no. 5, pp. 1587–1594, Oct. 2016.

[21] H. Taha, Z. Tang, T. Henneron, Y. Le Menach, J.-P. Ducreux, and F. Salomez, "Stabilized gauged formulation of Darwin model for FEM computation of industrial applications," *IEEE Trans. Magn.*, early access, Mar. 31, 2022, doi: 10.1109/TMAG.2022.3163893.

[22] S. Koch, J. Trommler, H. De Gersem, and T. Weiland, "Modeling thin conductive sheets using shell elements in magnetoquasistatic field simulations," *IEEE Trans. Magn.*, vol. 45, no. 3, pp. 1292–1295, Mar. 2009.

[23] A. Ospina, L. Santandrea, and Y. Le Bihan, "Electromagnetic field computation in magnetic and conductive thin sheets," *Sensor Lett.*, vol. 7, pp. 480–485, Jun. 2009.

[24] I. Cortes Garcia, S. Schöps, H. De Gersem, and S. Baumanns, "Systems of differential algebraic equations in computational electromagnetics," in *Applications of Differential-Algebraic Equations Forum*. Cham, Switzerland: Springer, 2018, pp. 123–169.

[25] L. Pace, N. Idir, T. Duquesne, and J.-C. De Jaeger, "Parasitic loop inductances reduction in the PCB layout in GAN-based power converters using S-parameters and EM simulations," *Energies*, vol. 14, no. 5, 2021, Art. no. 1495.

[26] "Code avancé de recherche en modélisation electromagnétique." Accessed: Dec. 8, 2021. [Online]. Available: https://code-carmel.univ-lille.fr/